ELSEVIER

Journal of Alloys and Compounds 266 (1998) 321–326

Journal of ALLOYS AND COMPOUNDS

Bulk and surface properties of crystalline and amorphous $Zr_{36}(V_{0.33}Ni_{0.66})_{64}$ alloy as active electrode material

Andreas Züttel*, Daniel Chartouni, Christof Nützenadel, Karl Gross, Louis Schlapbach

University of Fribourg, Physics Institute, Pérolles, CH-1700 Fribourg, Switzerland

Received 6 August 1997

Abstract

The electrochemical hydrogen absorption/desorption behavior of a crystalline and an amorphous $Zr_{36}(V_{0.33}Ni_{0.67})_{64}$ alloy sample was investigated. Electrodes made of the crystalline sample show a much lower resistance and consequently a higher discharge capacity compared to the electrodes made of the amorphous alloy. The XPS surface analysis did not explain the difference, we observed almost exactly the same depth profile on both samples. However the surface of the activated alloy compared to the non-activated was drastically changed. The oxide layer on an amorphous alloy seems to grow in a much more compact and stable structure than the oxide layer on a crystalline sample. © 1998 Elsevier Science S.A.

Keywords: Hydrogen storage alloys; Zr based alloys; Amorphorous alloys; Metal hydride electrode

1. Introduction

Most of the investigation on metal hydride alloys are done on crystalline phases. Crystalline alloys show a sharp phase transformation resulting in a change in the lattice constant during hydrogen absorption. The lattice mismatch at the interface between hydrided and the unhydrided phase leads, due to the brittleness of the material, to cracking of the larger alloy grains. Most alloys upon repetitive hydriding end up in a powder with a grain size distribution of a few micrometers. A crystalline alloy offers the hydrogen atoms well defined tetrahedral or octahedral interstitial sites. This leads to a very narrow binding-energy distribution for hydrogen. Since the chemical, electronic and geometric nature of the nearest neighborhood of an interstitial site mainly defines the binding characteristics for the hydrogen atom, the binding-energy of the hydrogen can be explained with the electronic band structure of the alloy. During hydrogen absorption a so-called hydrogen induced band is created about 6 eV below the Fermi-level and at the same time the Fermi-level moves up due to the additional electrons from hydrogen.

Amorphous alloys are usually produced as tapes which are a few micrometers thick [1]. Upon hydriding they do not break down into powder because there are a large number of different interstitial sites for hydrogen [2,3], and no spatial separation of the hydrided and unhydrided phase can be observed. This fact allows the investigation of amorphous alloy electrodes without adding any supporting material as it is necessary to contact crystalline powder. Furthermore, the absorption and desorption process does not change the surface area of the sample. Amorphous alloys generally exhibit a certain short range order like glass and should therefore be called metallic glasses. The short range order leads to the formation of interstitial sites similar to crystalline alloys of the same composition. However, the nearest neighbor atoms around the interstitial site are distributed in a statistical way. Harris et al. [4] propose that all A_xB_{1-x} metallic glasses, where A (B) is an early (late) transition metal, are structurally isomorphic and chemically random alloys which store hydrogen in tetrahedral interstitial sites A_nB_{4-n} (n=0, 1, 2, 3, 4). The sequence of site energy is determined by the number of late transition atoms Zr_4, Zr_3Ni, Zr_2Ni_2, $ZrNi_3$, and Ni_4 tetrahedral with increasing site energy (G_H=−40 kJ·mol^{-1}, −22 kJ·mol^{-1}, −4 kJ·mol^{-1}, 14 kJ·mol^{-1}, 33 kJ·mol^{-1} for 373 K [5]). The maximum absorbed hydrogen-to-metal atomic ratio within each type of interstitial site is

$$D(n) = 1.9\frac{4!}{n!(4-n)!}x^n(1-x)^{4-n} \quad (1)$$

independent of alloy and temperature. The factor 1.9 is the

*Corresponding author. Tel.: 0041 26 300 9086; fax: 0041 26 300 9747; e-mail: Andreas.Zuettel@unifr.ch

PII S0925-8388(97)00476-3

total number of tetrahedral sites per metal atom in the amorphous matrix which can be occupied by hydrogen, and is smaller than the total number of tetrahedral sites because of repulsion between hydrogen atoms at small distances. According to Kirchheim et al. [6] this factor varies between 1.2 and 1.7 depending on the A element size. The local modes of hydrogen vibration are not affected very much by filling different tetrahedral sites with hydrogen, whereas hydrogen diffusivity changes over two or three orders of magnitude. Kirchheim et al. [6] observed a diffusion coefficient of $D=10^{-8}$ cm$^2\cdot$s^{-1} for H/M=0.001 and $D=10^{-6}$ cm$^2\cdot$s^{-1} for H/M=0.3 on a $Zr_{35}Ni_{65}$ sample at 393 K. The diffusion coefficient at 273 K is approximately two orders of magnitude smaller depending on the hydrogen concentration. The concentration dependence of the diffusion coefficient is in semi-quantitative agreement with the model of constant saddle point energies and discrepancies may arise from correlation's between site and saddle point energies or from diffusion via sub lattices formed by the different types of tetrahedral. Aoki et al. [7] obtained the relative partial molar enthalpy and entropy for the absorption of hydrogen from the pressure–composition isotherms for both amorphous and crystalline $Zr_{37}Ni_{63}$ alloy. The quantities of the reaction enthalpy and entropy in the amorphous state show the minimum at certain hydrogen content (H/M=0.23, $\Delta H=-25$ kJ$\cdot$mol^{-1}, $\Delta S=-40$ J$\cdot$mol$^{-1}\cdot$K^{-1}) and they remain fairly constant as the hydrogen content is further increased. The characteristic variations in the reaction entropy for the amorphous Zr–Ni alloy may be attributed to the changes in the local environmental structure around hydrogen atoms, leading to an increase in the configuration entropy.

Varga et al. [8] observed no difference in storage capacity of nano- and micro-crystalline states, the maximal hydrogen content increases linearly with the Zr content in the $Ni_{1-x}Zr_x$ system (x=0.33, 0.36, 0.39, 0.41, 0.45 and 0.5). The storage capacity in the amorphous state is (H/M=1.1). Ciureanu et al. [9] found discharge capacities of batteries constructed using anodes manufactured from $Ni_{64}Zr_{36}$ rapidly quenched alloy fibers to be in the range from 220 to 260 mAh/g (10 h discharge rate).

In this paper we compare the electrochemical charge and discharge behavior of an amorphous and crystalline $Zr_{36}(V_{0.33}Ni_{0.67})_{64}$ alloy electrode and explain the differences with respect to the specific bulk and surface properties of the two samples.

2. Experimental

2.1. Alloy preparation

The $Zr_{36}(V_{0.33}Ni_{0.67})_{64}$ or $(Zr(V_{0.33}Ni_{0.67})_{1.778})$ alloy sample (6 g, ≈1 cm^3, M=191.02 g$\cdot$mol^{-1}) was prepared by r.f. levitation melting of the appropriate amounts of the elements, i.e. zirconium m(Zr)=2.8652 g from Goodfellow, 99.8% Zr, vanadium m(V)=0.9387 g from Koch-Light, 99.7% V, and nickel m(Ni)=2.1961 g from Johnson Matthey, 99.99% Ni. The elements were cut and cleaned from oxides with a file. The weight was adjusted on a single piece of every element by removing the excess amount with a file. The metals were then washed in acetone and subsequently introduced into r.f. levitation oven, vacuum (10^{-7} mbar). A copper crucible was used to hold the metals together before power was applied and levitation occurred. The metals were initially heated to 1480°C and they formed a homogeneous looking round ball. The power was reduced and the sample was held at 1350°C for 5 min. Thereafter the power was switched off and the sample was quenched to room temperature by contact with the water cooled crucible. We estimate the cooling rate to be in the order of 100°C/s. Half of the sample was ground into a powder (≈50 μm). The amorphous $Zr_{36}(V_{0.33}Ni_{0.67})_{64}$ sample was received from Bakonyi [10] as a tape approximately 3-mm wide and 20-μm thick.

2.2. Alloy characterization

X-ray diffraction was performed with copper radiation (Cu Kα λ=1.5406 Å). Channel width was set to $2\vartheta=0.1°$ and the angular resolution was found to be $2\vartheta=0.3°$ (FWHM). The count time was set to 100 s per channel resulting in a maximum count rate of approximately $1.5\cdot10^5$ counts on the main peak in the spectrum (0.3% error in the count rate).

2.3. Electrochemical tests

For the electrochemical measurements approximately 300 mg of the alloy powder was cold pressed (450 MPa) to a pellet (d=13 mm) between two expanded nickel screens. The pellets were connected to a nickel wire and squeezed between to nickel hydroxide electrodes separated by a non-woven polypropylene separator. The electrodes were charged and discharged electrochemically in a 30% KOH electrolyte in a cell open to the atmosphere. The potentials were referred to a mercury–mercury oxide electrode outside of the sandwich. The discharge cut-off potential was −0.6 V with respect to the Hg–HgO–OH$^-$ reference electrode. The electrodes were tested in a half-cell experiment with constant charge (10 mA, i.e. 30 mA/g) and discharge (10 mA, i.e. 30 mA/g) current. Upon 30 cycles the electrodes reached their maximum discharge capacity. The equilibrium potentials were measured in special cycles with charge and discharge pulses of approximately 5 mAh/g during the pause of the pulses (5 min) [11]. A set of electrodes were activated using a special pulse activation procedure. Pulse activation [12] means that the cell is connected to a potentiostat generating a rectangular po-

tential of −1.0 V and −1.7 V between the metal hydride electrode and the nickel hydroxide electrode. The pulse length is set to 50 s at each potential. This pulsing is repeated for 24 h at room temperature.

2.4. ESCA measurements

For surface analysis, the samples were rinsed with bi-distilled water, dried in air and pressed to a pellet and then introduced in the ultra high vacuum ($<10^{-8}$ Pa base pressure) of the spectrometer. The surface concentration of the elements was analyzed with X-ray photoelectron spectroscopy in a Perkin Elmer spectrometer.

3. Results and discussion

The crystallographic structure of the amorphous and the crystalline sample of $Zr_{36}(V_{0.33}Ni_{0.67})_{64}$ were determined by X-ray diffraction patterns (Fig. 1). The intensities were normalized to 100% for the peak maximum. The peak maximum on the main peak was $2 \cdot 10^5$ counts (crystalline sample). The crystalline alloy consists mainly of the C15 Laves phase (Fd3m, $MgCu_2$-structure, s.g. 227), however a minor part of the alloy formed the hexagonal C14 phase (P63/mmc, $MgZn_2$-structure, s.g. 194). The lattice constant of the cubic (C15) phase was found to be $a=7.12378\pm0.0005$ Å and for the hexagonal (C14) phase $a=5.0412\pm0.0005$ Å and $c=8.24831\pm0.0005$ Å. Four minor additional peaks at $2\Theta=39.848°$, $2\Theta=41.000°$, $2\Theta=58.403°$, $2\Theta=74.245°$ with an intensity of 7%, 5%, 3%, and 3%, respectively, could not be assigned. The amorphous alloy did not show any crystallinity.

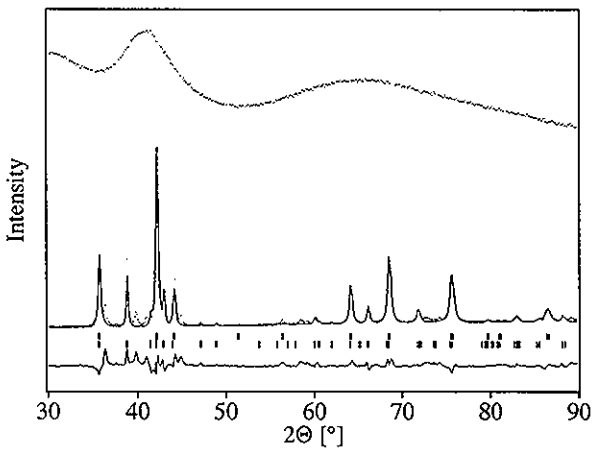

Fig. 1. X-ray diffraction pattern of the $Zr_{36}(V_{0.33}Ni_{0.67})_{64}$, amorphous sample on top, crystalline sample (measurement and fit), diffraction lines of the C15 phase, diffraction lines of the C14 phase, and difference spectrum on bottom.

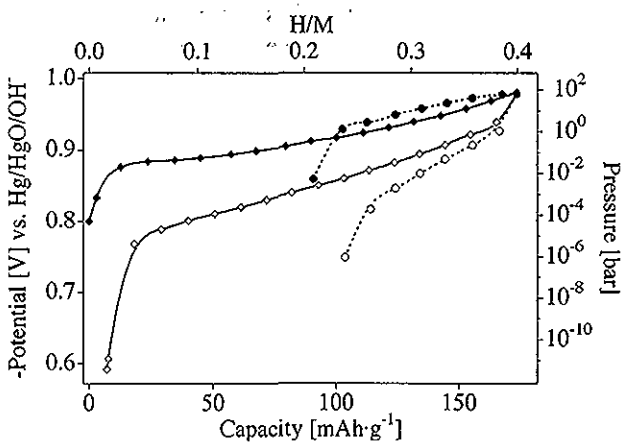

Fig. 2. Equilibrium curve of the crystalline (absorption ◆, disorption ◇) and amorphous (absorption ●, disorption ○) $Zr_{36}(V_{0.33}Ni_{0.67})_{64}$ sample. Charge and discharge currents were 15 mA/g and 0.75 mA/g for the crystalline and amorphous sample, respectively.

The electrochemically measured charge and discharge curves (potential measured while current was applied) of the amorphous and the crystalline alloy are shown in Fig. 2. We observed for the crystalline sample a discharge capacity of 170 mAh/g and 80 mAh/g for the amorphous sample. The applied currents were 15 mA/g for the crystalline and 0.75 mA/g for the amorphous sample. This setup allowed the potential curves of the two samples to overlap.

The comparison of the discharge capacity as a function of the discharge current is shown in Fig. 3. The discharge capacities decreases exponentially with increasing discharge current for both samples. However, the amorphous sample showed a much stronger decrease of the discharge capacity as a function of the discharge current. The following equation can be used to represent the discharge capacity (C) as a function of the discharge current (i):

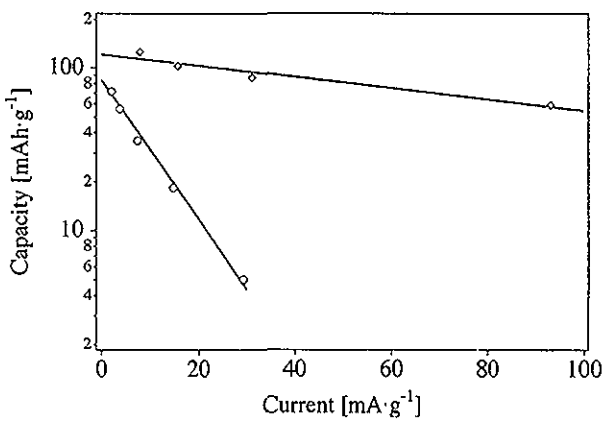

Fig. 3. Discharge capacity as a function of discharge current for the crystalline (◇) and amorphous (○) $Zr_{36}(V_{0.33}Ni_{0.67})_{64}$ sample.

$$C = C_0 \cdot 10^{-\beta i}. \quad (2)$$

The parameters were computed to be $C_0 = 121$ mAh·g^{-1} and $\beta = -0.0035$ g·mA^{-1} for the crystalline sample and $C_0 = 83$ mAh·g^{-1} and $\beta = -0.043$ g·mA^{-1} for the amorphous sample. Both electrodes have the same chemical composition and approximately the same geometrical surface area. The big difference in their rate capability has to originate in their different crystalline structure. The crystalline structure influences the hydrogen diffusion rate and the structure of the surface as well. Both are direct parameters of the rate capability.

The charge and discharge resistances of the electrodes are potential dependent. Fig. 4 shows the resistance measured by impedance spectroscopy of the amorphous and crystalline electrodes before and after activation as a function of the equilibrium potential, i.e. at different charge states. The initial resistance of an as-prepared electrode upon the first charge, measured at −1 V vs. Hg–HgO reference electrode, is very high and equals approximately 10 W for the crystalline electrode and 1000 W for the amorphous electrode. This resistance drops on the pulse activated samples to approximately 2 Ω for the crystalline electrode and to 150 Ω for the amorphous electrode. The resistance increases at more positive potentials for both electrodes. A drastic increase of the resistance was observed at approximately −0.8 V for the crystalline sample electrode. This potential corresponds to the potential for the oxidation of nickel ($E_0 = 0.110 - 0.0591 \cdot$pH [13] i.e. $E = -0.816$ V vs. Hg–HgO–OH$^-$) according to the following reaction.

$$Ni + 2OH^- \rightleftarrows NiO + H_2O + 2e^- \quad (3)$$

The equilibrium potentials as a function of the hydrogen contents together with the calculated density of states curve of the crystalline sample are shown in Fig. 5. The DoS curve shows a well defined but wide absorption peak corresponding to the sloping plateau. Due to the very high resistance of the amorphous sample, especially at lower potentials, it was not possible to measure an equilibrium curve on the amorphous sample electrode.

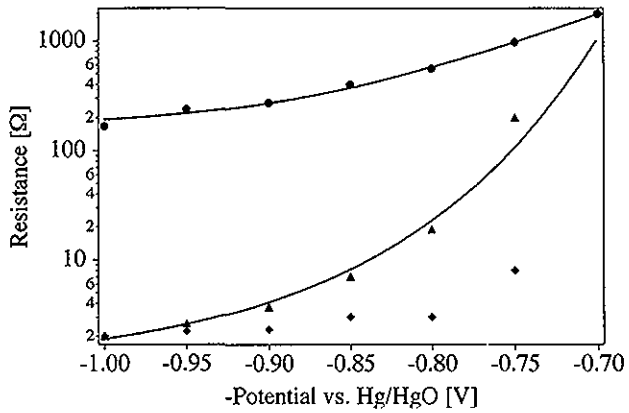

Fig. 4. Resistance as a function of the equilibrium potential for the crystalline and amorphous $Zr_{36}(V_{0.33}Ni_{0.67})_{64}$ electrodes: ◆ crystalline pulse activated electrode, ▲ crystalline cycle activated electrode and ● amorphous pulse activated electrode.

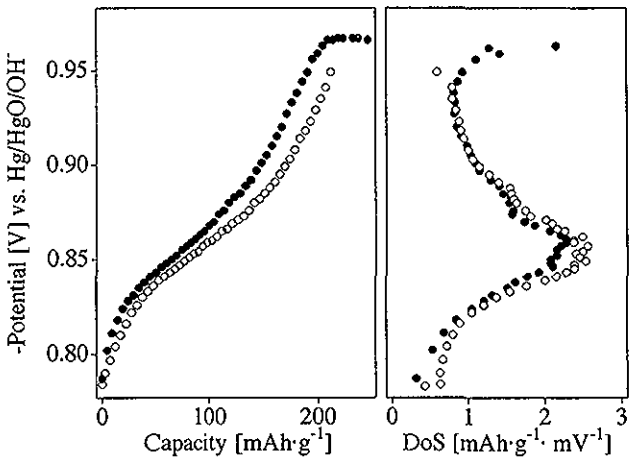

Fig. 5. Absorption (●) and desorption (○) equilibrium curve of the crystalline $Zr_{36}(V_{0.33}Ni_{0.67})_{64}$ sample on the left hand side and density of state curve on the right hand side.

The XPS depth profile of a freshly prepared electrode of the crystalline sample is shown in Fig. 6. The depth profile can be divided into three parts, the top surface (40 Å) is

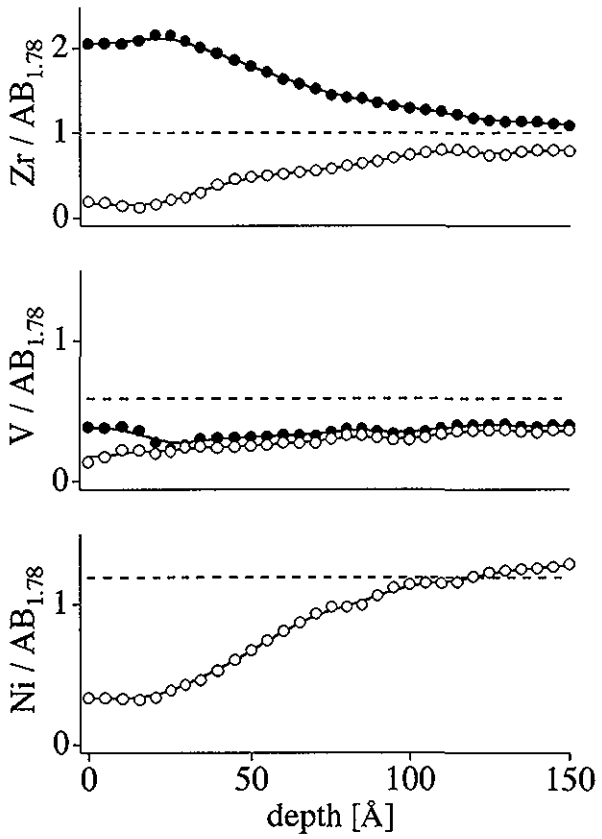

Fig. 6. XPS-depth profile for Ni, V and Zr of the as-prepared crystalline $Zr_{36}(V_{0.33}Ni_{0.67})_{64}$ sample. Filled markers represent the total amount of the element and empty markers represent the metallic part of the element. The sum of Ni, V, and Zr was normalized to 2.78 for ($AB_{1.78}$).

composed of zirconium oxide with small amounts of vanadium oxide and metallic nickel. Between 40 Å and 100 Å the composition changes smoothly to bulk composition and the elements become metallic. Beyond 100 Å the composition does not change further and corresponds to bulk composition. The XPS depth profile of the amorphous sample (Fig. 7) is very similar, except that the composition of the bulk is attained at a shorter distance into the sample. This is probably not a characteristic of the material but rather a property of the well defined geometric surface of the tape compared to the pressed powder pellet.

The surface composition of the pulse activated samples (Fig. 8) is very different from the surface composition of the freshly prepared electrodes. However, there was no difference found between the crystalline and the amorphous sample. The zirconium concentration corresponds to the bulk concentration and zirconium is oxidized down to more than 150 Å. The vanadium concentration is very low, indicating that vanadium dissolved into the electrolyte during the activation procedure. The nickel concentration is higher than bulk concentration, especially in the top layers (50 Å). However, more than half of the nickel was found to be oxidized down to 150 Å.

The XPS depth profile of the crystalline cycle activated electrode is almost the same as the depth profile of the pulse activated sample. This shows that pulse activation leads to the same changes in the surface composition as normal cycling of the electrode.

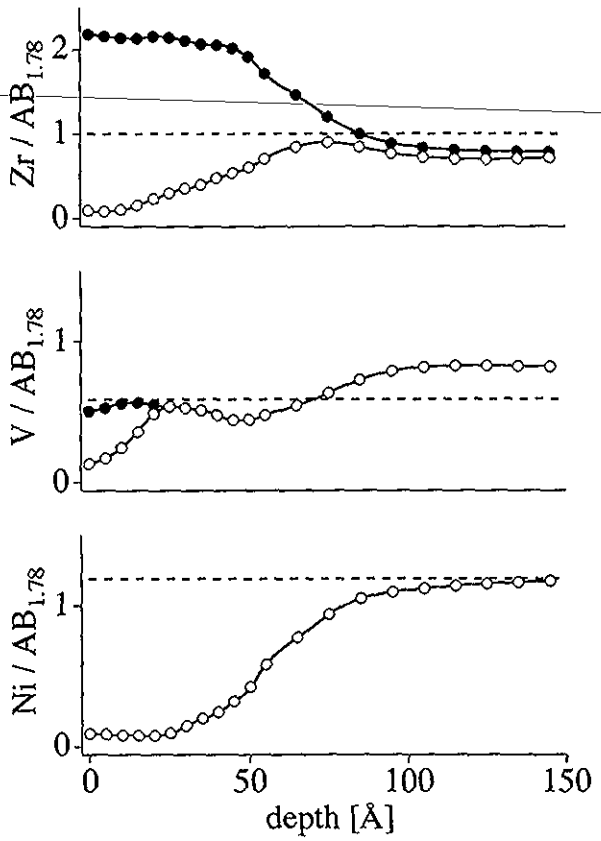

Fig. 7. XPS-depth profile for Ni, V and Zr of the as prepared amorphous $Zr_{36}(V_{0.33}Ni_{0.67})_{64}$ sample. Filled markers represent the total amount of the element and empty markers represent the metallic part of the element. The sum of Ni, V, and Zr was normalized to 2.78 for $(AB_{1.78})$.

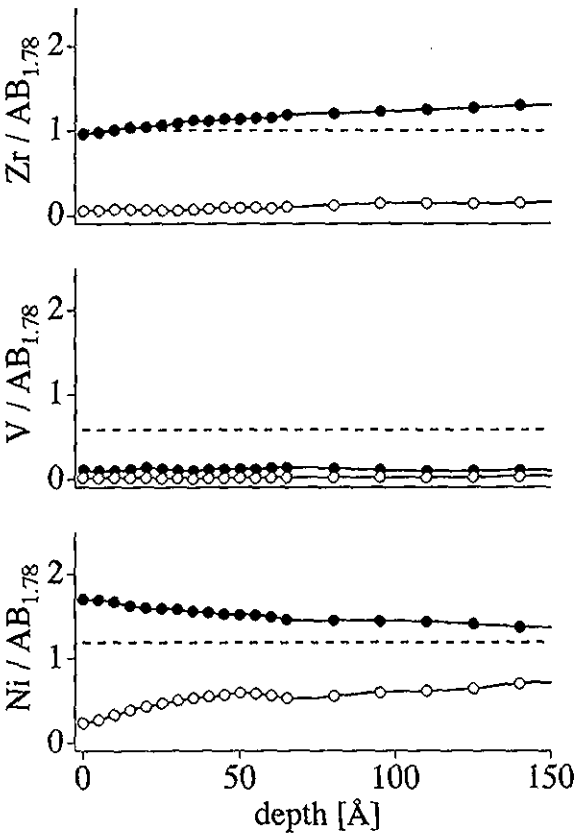

Fig. 8. XPS-depth profile for Ni, V and Zr of the crystalline $Zr_{36}(V_{0.33}Ni_{0.67})_{64}$ sample pulse activated electrode. Filled markers represent the total amount of the element and empty markers represent the metallic part of the element. The sum of Ni, V, and Zr was normalized to 2.78 for $(AB_{1.78})$.

4. Conclusion

In electrochemical tests, we observed different reversible capacities and rate capabilities in the amorphous and crystalline sample. The much lower capacity of the amorphous sample can be explained by the smaller number of appropriate interstitial sites. The lower rate capability is explained by the formation of a more dense and passivating surface oxide layer. The oxide layer is more stable on an amorphous substrate compared to a crystalline substrate. This is due to the smoother interface between the oxide and the amorphous metal and the missing stress in the alloy during hydriding because of the lack of an α–β-phase interface.

Acknowledgements

Support with the amorphous sample by Imre Bakonyi and the crystalline sample by Felix Meli is acknowledged.

References

[1] I. Bakonyi, I. Nagy, E. Tóth-Kádár, M. Hossó, K. Tompa, G. Konczos, A. Lovas, J. Less-Common Met. 172–174 (1991) 899–907.
[2] F.H.M. Spit, J.W. Drijever, S. Radelaar, Z. Phys. Chem. 116 (1979) 225.
[3] F.H.M. Spit, J.W. Drijever, S. Radelaar, Scripta Metall. 14 (1980) 1071.
[4] J.H. Harris, W.A. Curtin, M.A. Tenhover, Phys. Rev. B 36(11) (1987) 5784–5797.
[5] F. Jaggy, W. Kieninger, R. Kirchheim, Z. Phys., Chem. N.F., Bd. 163 (1989) 431–436.
[6] R. Kirchheim, W. Kieninger, X.Y. Huang, S.M. Filipek, J. Rush, T. Udovic, J. Less-Common Met. 172–174 (1991) 880–889.
[7] K. Aoki, M. Kamachi, T. Masumoto, J. Non-Cryst. Solids 61–62 (1984) 679–684.
[8] L. Varga, A. Lovas, K. Tompa, J. Joubert, A. Percheron-Guegan, J. Alloys Comp. 231 (1995) 321–324.
[9] M. Ciureanu, J.O. Ström-Olsen, D.H. Ryan, P. Rudkowski, G. Rudkowska, B. Bondoc, J. Electrochem. Soc. 141(12) (1994) 3291–3295.
[10] Imre Bakonyi, Central Research Institute for Physics, POB 49, H-1525 Budapest (Hungary).
[11] A. Züttel, F. Meli, L. Schlapbach, J. Alloys Comp. 206 (1994) 31–38.
[12] M. McCormack, M.E. Badding, B. Vyas, S.M. Zahurak, D.W. Murphy, J. Electrochem. Soc. 143(2) (1996) L31–L33.
[13] Atlas of Electrochemical Equilibria in aqueous solutions by Marcel Pourbaix, Pergamon Press, Oxford, 1966, pp. 330–334.